E3S Web of Conferences **663**, 01012 (2025) https://doi.org/10.1051/e3sconf/202566301012
IGTC 2025

AM ENABLED INJECTION SYSTEMS FOR ENHANCED FUEL FLEXIBILITY

Vicente Rubio [1], *Jihwan Ahn*[1], *Clemens Maucher*[2], *Hans-Christian Möhring*[2], and *Fabian Hampp*[1,*]

[1]Institute of Combustion Technology for Aerospace Engineering, University of Stuttgart, Pfaffenwaldring 38-40, 70569 Stuttgart, Germany

[2]Institute for Machine Tools, University of Stuttgart, Holzgartenstraße 17, 70174 Stuttgart, Germany

Abstract. The demand for fuel-flexible combustion systems is rising with the transition to renewable energy vectors like hydrogen, ammonia, methanol, sustainable aviation fuel (SAF), and hydrogenated vegetable oils (HVO). High-momentum jet-stabilised combustion systems have shown significant benefits for hydrogen-based operation. However, achieving clean, fuel-flexible combustion imposes strict requirements on injection and mixture formation, especially as partially cracked ammonia can cause large variations in the Wobbe index, affecting fuel momentum and penetration depth. Decoupling mixture formation from fuel properties is key to ensuring homogeneous mixing before flame interaction. Additive manufacturing (AM) offers innovative solutions by enabling intricate fuel injection designs. This study explores AM-enabled space-filling injectors to enhance fuel flexibility, focusing on Powder Bed Fusion Laser Beam (PBF-LB/M) processes in In718 to create space-filling micro-structures with sub-100 µm feature sizes. The objectives are optimised fuel placement and mixture homogenisation while realising fuel jet injection momentum independence. Using schlieren imaging, the improved mixture formation with reduced Wobbe index sensitivity is demonstrated, enabling excellent multi-fuel adaptability. This research highlights AM's potential in developing cost-effective, multi-fuel injection systems for gas turbines, particularly in applications requiring co-firing and adaptability to regional or temporal availability fluctuations of sustainable carbon-free energy vectors.

1 Introduction

Due to the intermittency of renewables, backup energy sources are required. In this context, clean and fuel flexible gas turbine (GT) combustion systems can offer the required dynamic response to load demands and low emissions. However, the rise of a wide range of carbon-free energy vectors leads to stringent fuel flexibility requirements of modern GT burners. The physical and chemical fuel properties inherently influence mixture formation, combustion processes, and emission formation [1]. In order to achieve the required fuel flexibility and multi-fuel co-firing with simultaneous control over emission mitigation strategies, decoupling of mixture formation from the combustion process is highly beneficial. This facilitates fuel independent mixture stratification mitigation strategies, i.e. avoiding local hot spots and fuel rich regions, and thereby reducing pollutant formation, i.e. NO_X and soot.

Fuel variability has a strong influence on the combustor's operability, and can lead to challenging behaviours such as flashback, blowout, autoignition and combustion instabilities [2]. Current studies focus on the usage of fuels ranging from CH_4 and higher hydrocarbons (e.g. C_2H_6, C_3H_8), synthesis gas (H_2/CO blends), CH_4/H_2 or CH_4/NH_3 blends, to pure H_2 and pure NH_3 [3]. Hydrogenated vegetable oils (HVO), sustainable aviation fuels (SAF) [4] and oxygenated fuels (e.g. glycerol, methanol) [5] are studied as viable liquid fuel options. As shown in Table 1, the selected gaseous fuels readily present a very wide range of physical and chemical properties. These induce very different combustion processes and technical challenges. Traditionally, the development of GTs is based on natural gas (or CH_4 as surrogate) and higher hydrocarbons combustion. The use of carbon-neutral fuels is essential to decarbonise GT combustion, ideally without introducing severe hardware modifications, with distinct challenges. H_2 combustion can suffer from instabilities, increased volumetric injection flow rates due to the low energy density, flashback and high autoignition risk, added to transportation and storage challenges [6]. On the opposite side of the considered fuel spectrum, NH_3 is characterised by ignition difficulties, low flame speed and flame quenching, as well as high NO_X emissions and NH_3 slip [7]. In this context, fuel blending aims to palliate the individual fuel challenges, making them an attractive option [8]. Established combustion techniques that focus on homogeneous fuel/air mixing and excel on fuel flexibility include moderate or intense low oxygen dilution (MILD) [9] and flameless oxidation (FLOX) [10]. Both rely on exhaust gas recirculation and combustion under diluted conditions. In contrast to

* Corresponding author: fabian.hampp@ivlr.uni-stuttgart.de

traditional flamelet combustion behaviour, this leads to autoignition, a homogenised temperature field, and extended lean combustion operability. However, for NH_3, fuel NO_X emissions decrease under fuel-rich rather than lean conditions, yet cause an increase of unburnt NH_3 [11]. Hence, staged rich-quench-lean combustion appears as a promising solution, reducing unburnt fuel without significantly increasing NO_X [7]. Micro gas turbines (MGTs) (30–250 kW) [12] include additional challenges such as low residence time for mixing and heat release [13]. In this context, lean premixed combustion and micro-mixing offer a promising solution to fuel property variations. Therefore, it is essential to design low pressure drop, compact and efficient injector systems capable of achieving spatially and temporally homogeneous mixtures. Micro-mixing injection concepts, acting as an intermediate between premixed and non-premixed combustion, show promising results. Several studies have examined jet-in-crossflow (JiCF) micro-mixers (0.25–1 mm pores) [14-22] for various fuel types, revealing that micro-injection systems can approach premixed emission levels.

Previous studies on micro-mixing injection systems mostly use a limited number of JiCF injectors, constrained by traditional manufacturing challenges [23,24]. Subtractive methods (e.g., milling, turning) restrict complex, space-efficient injector designs, preventing full decoupling of the injection performance from physical fuel properties. Additive Manufacturing (AM) overcomes these limitations by enabling layer-by-layer fabrication, optimising design, performance, and energy efficiency [25]. Among AM techniques, this study focuses on PBF-LB/M, which selectively melts metal powder layers, leveraging microchannels and porous media to improve fuel distribution and mixing. Maucher et al. [26] achieved 100-300 µm pore sizes in Inconel 718 for porous fuel injection. Bhayaraju et al. [27] demonstrated improved stochastic fuel mixing and stability on porous media injection using PLIF/PIV analysis. Kang et al. [28] fabricated an airblast injector with ≤ 55 µm slits, confirming the feasibility of stochastic and deterministic micro-structures via PBF-LB/M. The study highlighted AM process parameters for refining surface roughness and fuel control. Admou et al. [29] validated AM-based micro gas turbine combustion chambers, proving lower emissions and peak temperatures but with a higher pressure drop, highlighting that AM can significantly enhance MGT injection system performance.

The current study expands the work of Maucher et al. [26] and Kang et al. [28] by further optimising the design of micro-channel (400 µm) structures, porous media and micro-pores (200 µm). The method is used to develop space-filling concepts to enhance the spatial distribution of injection ports and thereby decouple the mixing process from physical fuel properties and injection momentum. The injector designs will be analysed using schlieren imaging [30] and pressure drop analysis with focus on the mixing performance. Section 2 discusses the used methodology for the manufacturing of the selected injectors, followed by a detailed explanation of the experimental setup in Sec. 3 and finally, before concluding, the analysis of the experimental data is presented in Sec. 4.

Table 1: Preferred gaseous fuel comparison at 1 atmosphere, room temperature and stoichiometric conditions [31, 32] and Wobbe index comparison $Wi = HHV/\sqrt{S_g}$ [33, 34], where S_g is the specific gravity of the gas.

	H_2	NH_3	CH_4
Lam. flame speed (m/s)	2.91	0.07	0.37
Flammability range (%v)	4-75	15-28	5-17
LHV (MJ/m^3)	10.8	15.6	35.8
HHV (MJ/m^3)	12.8	18.6	39.8
Density (kg/m^3)	0.089	0.682	0.717
Autoignition T (K)	773	924	853
Wobbe index (MJ/m^3)	47.5	24.9	52.0

2 Additive manufacturing

The additive manufacturing is conducted using a PBF-LB/M Trumpf TruPrint 1000. As powder material, In718 from Carpenter Technology Corporation with particle size distribution of d_{10} = 24 µm, d_{50} = 36 µm and d_{90} = 47 µm is used. The key printing parameters, derived from Maucher et al. [26] and Kang et al. [28], are summarised in Table 2.

Table 2. Printing parameters for the PBF-LB/M TruPrint 1000 machine with In718 powder.

Parameter	Value
Laser power	75 W
Scanning speed	1000 mm/s
Layer height	20 µm
Laser spot size d_s	30 µm
Shielding gas	Argon
Contour offset	35 µm

Moreover, two distinct printing strategies have been used, as detailed in Table 3. The first one, termed "solid", has been used for all non-permeable walls and the second one termed "porous" for the creation of permeable walls allowing to tailor the porosity (ε). For solid elements, the hatch distance, defined as the ratio between the adjacent laser paths distance (d_h) divided by the melt pool width (d_s), must be small enough so that consecutive welded paths overlap, achieving a porosity of close-to nil. According to Maucher et al. [26] and Kang et al. [28], the best printing strategy for thin and solid walls is achievable by a layer rotation of α = 67° and a contour-first approach. This allows to create fully dense walls with close-to isotropic material properties. On the other hand, the realisation of permeable structures requires a significantly larger d_h, introducing stochastic gaps, while keeping the structural integrity of the sample. A-priori testing (Fig. 1) determined the optimal hatching distance with a porosity of ε = 0.32.

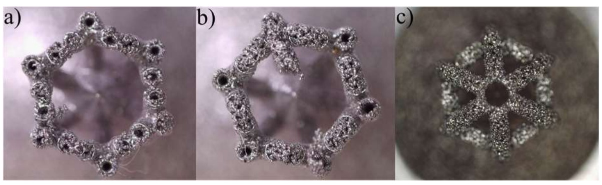

Fig. 1: Porous d_h iteration study. a) d_h/d_s = 13, b) d_h/d_s = 10. c) d_h/d_s = 8. The latter settings are used to create the porous caps in the present study, realising a nominal porosity of ε = 0.32.

Table 3. Selected parameters for the different printing strategies, where α is the layer rotation angle, b the build-up direction, d_h/d_s the normalised hatch distance, ε the porosity.

Case	α (°)	b	d_h/d_s	AM seq.	ε
Solid	67	V	1.3	C	0
Porous	67	V	8	H	0.32

3 Experimental setup

In the following, the burner facility and diagnostics are introduced in addition to the operating condition and data reduction methodology.

3.1 Burner facility

A schematic of the single-nozzle Piloted Jet Ammonia Burner (PJAB), including a flow diagram with labels, is shown in Fig. 2. A detailed description of the spray burner variant is provided by Kang et al. [35]. Key components include the air plenum and contraction nozzle, the central fuel supply and injection system, the cylindrical combustor nozzle, and the pilot and shield air assembly. The combustion air is regulated by a calibrated Brooks mass flow controller (Brooks Instrument SLA5800 series) and can be heated up to 800 K using a PID-controlled electric inline heater (Tutco SureHeat F076418). A second identical heater is installed to either preheat the pilot air or to operate a heat exchanger to preheat the fuel. High temperature heated hoses (Hillesheim H 900 series) transport the preheated air to the burner assembly. The combustion air is decoupled from inflow conditions by means of multiple deflections and a porous plate. The adjoining contraction nozzle reduces the diameter from 60.0 mm to 8.0 mm adhering to wind channel design guidelines to minimise flow separation. The combustor nozzle reduces the diameter conically over a length of 16.0 mm from 8.0 mm to the final combustor nozzle diameter (D) of 6.0 mm. The cylindrical section of the combustor nozzle has a length of 33 mm (i.e. 5.5 D). The preheated combustion air flows upward through the nozzle at a bulk velocity (u_b). The air temperature is regulated with a k-type thermocouple and the pressure is monitored via a transducer (GEMS 3500, 0-2.5 bar), both installed within the contraction nozzle.

Each fuel component is controlled by means of an individual calibrated Brooks mass flow controller. The fuel components are blended using a static mixer and transported via a temperature controlled central supply lance into the contraction nozzle. The injectors are mounted onto the fuel supply lance tip using compression fittings to create a leak-tight seal. For centralisation within the combustor nozzle, the injectors are further equipped with three circumferentially equal-spaced winglets. The axial position of the injection point can be seamlessly adjusted by retracting the fuel supply lance to realise direct injection (i.e. non-premixed condition with 0.0 mm mixing length) to close-to fully premixed conditions. The fuel supply pressure is monitored using a 2nd transducer (GEMS 3500, 0-2.5 bar) in the static mixer upstream of the fuel supply lance.

A co-annular pilot burner surrounding the central main nozzle delivers a continuous heat source. A perfectly premixed gas blend of 80% hydrogen and 20% methane with air at an equivalence ratio of $\Phi = 0.55$ provides the vitiated co-flow of hot combustion products with an adiabatic flame temperature of 1647 K. The gases are mixed inside an additively manufactured static mixture and fuel distributor assembly that also acts as flashback arrestor. The pilot mixture is supplied to the plenum using multiple inclined slits and circumferential holes. The pilot plenum is enclosed by an additively manufactured Inconel 718 porous plate, on which the pilot flames are anchored. Depending on the bulk velocity and flame anchoring process, this leads to heat losses into the porous plate of 200 – 400 K. The AM porous plate is equipped with thermocouples to monitor its temperature for early flashback warning and to determine the heat loss of the pilot flame. The pilot is further stabilised by the shield air flow, supplied through a porous plate ring, preventing ambient air entrainment.

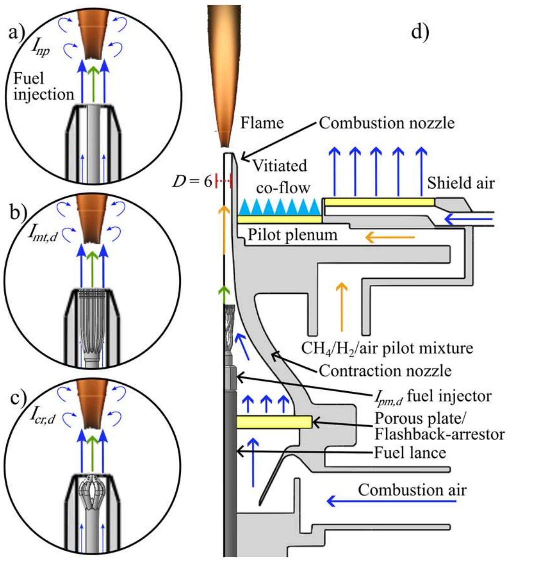

Fig. 2: Zoomed version of the direct injection configuration for (see Table 4). a) I_{np}. b) $I_{mt,d}$. c) $I_{cr,s}$. d) Simplified sketch of the burner for technically premix configuration.

3.2 Diagnostic setup

Schlieren imaging is a powerful optical technique to visualise the mixing process evolution of gases with different refractive indices, making it ideal for investigating fuel-air interactions in turbulent flows (e.g. Settles and Hargather [30]). In this work, a high-speed Nd:YAG laser (10 kHz, 532 nm) is utilised as light source. The laser beam is directed into a dye laser flow cell, circulated by a Rhodamine 6G and ethanol solution. An approximate point light source of the resulting fluorescence is created by placing a 500 µm precision pinhole directly in front of the cuvette quartz glass wall. The broadband light is collected and collimated using a plano-convex lens (Ø 50.8 mm, focal length: 80 mm). The collimated light is then passed through the interrogation region and recollected using a 2nd plano-convex lens (Ø 100 mm, focal length: 300 mm). The refractive index gradients caused by gas mixture stratifications create deflections. A vertically positioned knife-edge in the focal point of the last lens enhances the contrast of the refraction index gradients, thereby revealing fine structures in the mixing process. For visualisation, a high-speed Photron SA5 camera, equipped with a 200 mm Nikon macro lens (f/4.0), is used and synchronised with the laser by means of a programmable timing unit (PTU X, LaVision). While the quantification of mixture fraction via schlieren techniques is feasible [36], robust calibration in a turbulent multi-layer jet, with and without heat release from combustion, is far from trivial. Therefore, schlieren imaging is here used to semi-quantitatively analyse mixture homogenisation in relation to a fully premixed case. Although no quantitative mixture fraction values can be derived, the current data can serve as validation target for corresponding CFD simulation. For this purpose, mixing length scales are determined, which are crucial for the design optimisation of fuel-flexible systems.

3.3 Data reduction approach

In order to provide a semi-quantitative comparison of the mixing performance of the developed AM injection systems, the following post-processing is conducted:

1. Subtraction of the average white image (J_w - recorded in the absence of flow) from the instantaneous schlieren images (J_i), yielding J_c.
2. Determination of image gradients on the basis of J_c by means of a Scharr filter [37] in *x* and *y*-direction as well as with a 2D kernel.
3. Super-pixel generation with 10×10 pixel² binning.
4. Ensemble compilation of the schlieren image intensities and gradients in all super-pixel over all 5000 J_c into a predefined histogram with 100 bins.
5. The result is a 4D array with dimensions (super-pixel in *y*, super-pixel in *x*, bins, methods).

Subsequently, the histogram in each super-pixel is analysed and changes in the distribution shape provide insights into the mixedness. For example, the standard deviation of the gradient distribution is here used to visualise the co-existence of sharp refraction index gradients, e.g., between different gases, and, in the limit, plateaus within unmixed streams. By contrast, a narrow standard deviation (σ) is indicative of homogeneous and smooth gradients, as evident in a fully premixed case.

3.4 AM enabled fuel flexible injectors

This study builds upon the work of Maucher et al. [26] and Kang et al. [28], further refining micro-channel (400 µm) and micro-pore (diameter 100 – 300 µm) structures to advance the fuel flexibility and mixture homogenisation of injection systems. The designed injectors (*I*) can be categorised into three groups, see Table 4. The non-premixed reference injector (I_{np}) is provided by single straight pipe with inner and outer diameter of 2.0 and 3.0 mm, respectively.

The second group consists of space-filling micro-injectors (see Fig. 2b-c) with an outer diameter of, or just below, 6.0 mm at the tip to facilitate direct injection. The fuel is initially supplied through a tube with an inner diameter of 2 mm and subsequently distributed through micro-channels to the injection points to minimise the pressure loss. Two sub-categories are created. The first one consists of an array of 19 micro-tubes (I_{mt}, Figs. 2b and 3a-c) with an outer and inner diameter of 800 and 400 µm, respectively. The second design exhibits a crown-like shape (I_{cr}, Figs. 1, 2c and 3d), consisting of 6 curved tubes with outer and inner diameter of 1.2 mm and 800 µm, respectively. Both sub-categories are manufactured in a jet-in-crossflow (JiCF) approach with a defined number of 250 µm spatially distributed deterministic holes (Fig. 3b). The second approach is surface injection, realised by adding porous media (PM) caps onto the micro-tubes and thereby creating a close-to stochastic distribution of arbitrary injection micro-holes (Fig. 3a). The former approach is identified by subscript d – deterministic and the latter by subscript s – stochastic. For all designs, the injection extends over a length of 2.0 mm on the cylinder surface (see Fig. 3).

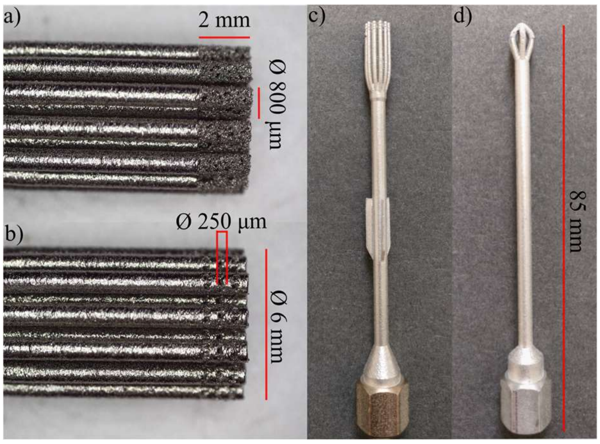

Fig. 3: Macro view of AM space-filling micro-tube injector with (a) porous media surface injection ($I_{mt,s}$) created with d_h/d_s = 8 and (b) deterministic holes ($I_{mt,d}$); Global view of AM space-filling c) micro-tube injector ($I_{mt,d}$) and d) crown-type injector with porous media surface injection ($I_{cr,s}$). Its macro view is depicted in Fig. 1c.

Finally, the third injector group represents the fully-premixed case (I_{pm}), see Fig. 4, that is recessed upstream into the contraction nozzle (see Fig. 2d). For that, a significantly shorter, fractally distributed, space-filling injection concept with a total of 48 injection branches is utilised. The outer and inner diameter of each injection branch is 800 and 400 µm, respectively. This design is manufactured in the JiCF and surface injection approach, yet only the former is used in the current study as mixture quality differences have not been measured.

These designs leverage and push current AM capabilities in creating novel injection systems, while always maintaining the blockage ratio to the combustion air below 30% (i.e. the straight pipe reference injector exhibits a blockage ratio of 25%). The first hypothesis behind the designs is, that by spatially distributing the injection points, in the limit to a surface injection realised by the porous caps, and by enlarging the injection area, the fuel placement becomes independent of the injection momentum (i.e. fuel mass flow rate and density). The mixture homogenisation is consequently only dependent on the spatial distribution of the injection points and turbulent mixing and is thereby broadly decoupled from physical fuel properties, creating excellent fuel and operational flexibility. Prompt mixture homogenisation in a direct injection configuration (i.e. approximating fully premixed conditions prior to the flame front) creates the foundation for advanced emission control strategies while fulfilling safety-related requirements due to operation with hydrogen. The second hypothesis is, that due to the sheer number of injection holes, the AM process inherent tolerances and inaccuracies become statistically well distributed, thereby mitigating their influence on local mixture stratification. These hypotheses are tested by means of schlieren imaging and pressure drop experiments. The specifications of all injection systems are further expanded in Table 4.

The injections systems (with exception of I_{pm}) are installed in a direct injection (DI) configuration. First, this allows to assess the entire mixing process and creates the most adverse conditions in terms of mixture homogenisation. Moreover, and specially with H_2 in high preheat conditions, boundary layer flashback within the mixing duct is a significant concern [38]. Hence, reducing the reactivity within the boundary layer, e.g., by substantially reducing the mixing length in the limit to direct injection, can mitigate the risk of related flashback events due to the absence of combustible mixtures in low strain and flow regions [39]. In addition, the comparatively high air flow velocities induce significant shear and dissipation of radicals, further mitigating the risk of flashback and flame anchoring in related combustion processes.

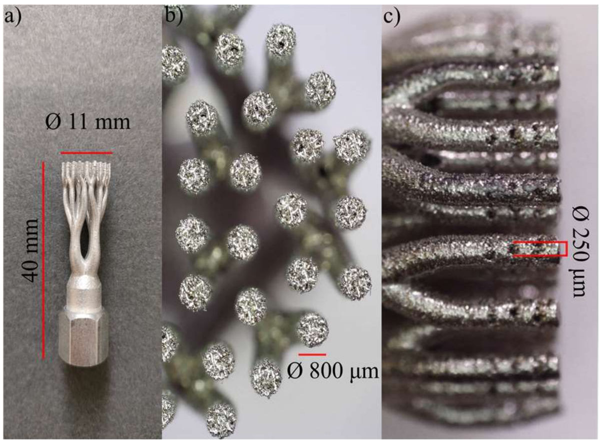

Fig. 4: Fully premixed reference injector I_{pm}. a) Side view $I_{pm,s}$. b) Zoomed top view $I_{pm,s}$. c) Zoomed side view $I_{pm,d}$.

Table 4. Injector overview. Name provides the nomenclature, Inj. the injection strategy with PM – porous media caps with surface injection, JiCF – jet-in-crossflow injection, J is the momentum flux ratio [40] for the entire operating condition variation and A is the nominal injection area.

Case	Name	Inj.	J (N) [x10^{-2}]	A (m^2) [x10^{-5}]
Non-premixed	I_{np}	Jet	0.98-178	0.31
Space-filling	$I_{mt,s}$	PM	0.007-1.5	3.06
	$I_{mt,d}$	342 JiCF	0.02-4.9	1.68
	$I_{cr,s}$	PM	0.005-0.95	4.35
	$I_{cr,d}$	48 JiCF	1.6-325	0.24
Fully premixed	$I_{pm,s}$	PM	0.003-0.52	7.72
	$I_{pm,d}$	864 JiCF	0.009-1.7	4.24

3.5 Operating conditions

Non-reactive mixture homogenisation is investigated, i.e. pilot and shield streams are operated using air only and the main nozzle mixture is not ignited. The main combustion air temperature is maintained at 293 K. To minimise the amount of unreacted fuel being dumped into the exhaust, the fuel mass flow rate is set, stationary conditions achieved, the high-speed schlieren measurements conducted and the fuel valves closed immediately afterwards. In the current study, the bulk flow velocity (u_b), the fuel type (H_2, CH_4) and the fuel mass flow rate (i.e. equivalence ratio Φ) are varied as listed in Table 5. This variation is conducted with all injection systems listed in Table 4.

Table 5. Overview of the conducted operating condition variation for each injector, where u_b is the bulk velocity, Φ is the equivalence ratio, $\dot{m}$ is the fuel mass flow rate and J is the momentum flux ratio [40], expressed as the range between the minimum and maximum values from all injector models.

OC	u_b (m/s)	Φ	$\dot{m}$ (g/s)	J (N) [x10^{-2}]	Fuel
1	40	0.2	0.014	0.003—1.6	CH_4
		0.6	0.040	0.02—14.2	
		1.0	0.064	0.06—39.1	
		2.0	0.118	0.26—160	
2	40	0.2	0.007	0.006—3.6	H_2
		0.6	0.017	0.05—28.6	
		1.0	0.025	0.13—79.5	
		2.0	0.039	0.53—325	
3	80	0.2	0.013	0.005—3.1	H_2
		0.6	0.034	0.05—28.6	
		1.0	0.050	0.13—79.5	
		2.0	0.077	0.51—317	
4	120	0.2	0.020	0.005—3.3	H_2
		0.6	0.051	0.05—28.6	
		1.0	0.075	0.13—79.5	
		2.0	0.116	0.52—319	

4 Results and discussion

In the following chapter, the performance of the different AM enabled fuel injection systems is first described via schlieren images of non-reactive flows, followed by detailed discussion on the mixing performance and pressure drop data.

4.1 Schlieren images

The schlieren imaging provides a clear visualisation of the refraction index gradients and in the present iso-thermal case thus mixture strification (see Fig. 5). The injector tips are positioned 4.0 mm downstream of the combustor nozzle exit to capture the entire distribution of injection holes or surface. Injector I_{np} (Fig. 5a) shows a typical co-annular H_2 jet injection into cold air with u_b = 120 m/s, Φ = 2.0. The deep axial jet penetration is self-evident, resembling the limiting case of a non-premixed system. In comparison, the second limit is provided by means of a fully premixed system using $I_{pm,d}$ (Fig. 5f) that is installed $> 10\,D$ upstream of the combustor nozzle exit. The residual schlieren originate from the turbulent H_2 / air jet penetrating into the pure air co-flow. These residual fine-scale gradients render a quantitative delineation of the mixture fraction variation error-prone and are thus omitted here. The space-filling injectors are naturally situated in between due to the sheer number of injection ports.

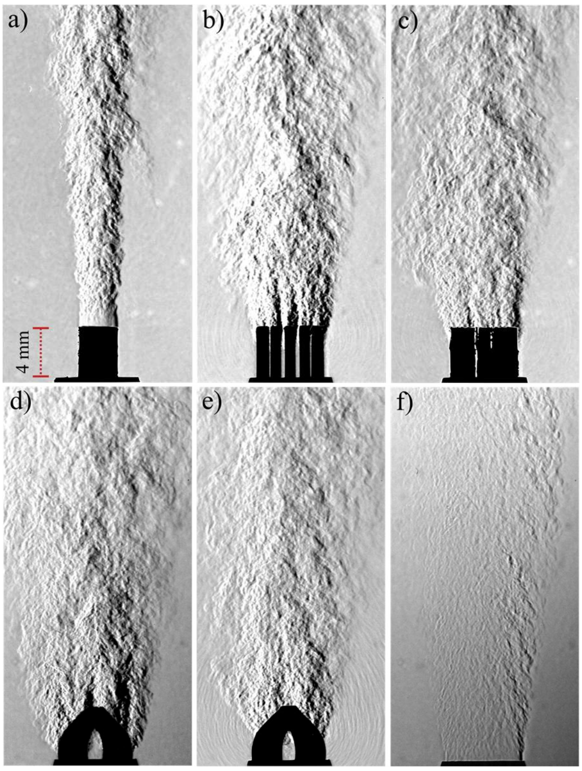

Fig. 5: Instantaneous schlieren images with subtracted average background (J_c) for H_2 with u_b = 120, Φ = 2.0: Injectors a) I_{np}. b) $I_{mt,s}$. c) $I_{mt,d}$. d) $I_{cr,s}$. e) $I_{cr,d}$ and f) $I_{pm,d}$.

The micro-tube family with stochastic porosity and deterministic JiCF holes show a very similar qualitative behaviour. This can be attributed to the high number of 342 and spatial distribution of JiCF holes in $I_{mt,d}$ (Fig. 5c). This basically approximates readily a surface injection as realised in $I_{mt,s}$ (Fig. 5b) with the porous caps. The nominal injection area is up to one order of magnitude higher than the reference case I_{np}. This leads, in combination with the JiCF arrangement, to a significantly enhanced fuel dispersion.

The I_{cr} family shows an even more pronounced radial dispersion directly adjacent to the injection point. Nevertheless, due to the notably different effective injection area (see Table 4), stronger differences can be observed in the near field of the stochastic porous media surface injection in comparison to the deterministic JiCF. Injector $I_{cr,s}$ (Fig. 5d) realises a wider fuel distribution and no jet behaviour whereas injector $I_{cr,d}$ (Fig. 5e) shows small jet structures and a reduced initial spread angle. All space-filling AM injection systems show a very high degree of axial symmetry, which implies that both, the stochastic porous media as well as the deterministic JiCF manufacturing approach, realise statistical homogeneity during the injection process.

4.2 Mixing performance

A semi-quantitative mixing performance evaluation of the AM space-filling injection systems is conducted next. Therefore, the mixture homogeneity is assessed based on the distribution width (i.e. standard deviation) of the schlieren image intensity gradients and compared against the non-premixed and fully premixed reference cases. This visualisation technique is chosen as the fully premixed case realises a close-to horizontal line when plotting the standard deviation of the gradient distribution ($\sigma_{\nabla J_c}$) as a function of axial distance from the combustor nozzle exit (see dashed line in Fig. 6). It is worth noting, that two unmixed streams also create a very narrow spread and thus low values of $\sigma_{\nabla J_c}$. The latter is relevant mostly for the non-premixed cases. Figure 6 depicts $\sigma_{\nabla J_c}$ for the entire operating condition and injector variation as a function of axial distance from the combustor nozzle exit (z) along the burner symmetry axis (i.e. $x = y = 0.0$ mm). The injectors are installed so that the tip is positioned at $z = 4.0$ mm, realising injection in the space-filling concepts from z = 2.0 – 4.0 mm to visualise the entire fuel injection process (see also Fig. 5). The different fuels and bulk velocities are depicted in separate columns and the different equivalence ratios in separate rows from lean to rich (top to bottom). The residual gradient distribution width of the fully premixed case (I_{pm}) stems from the interaction of the premixed jet with surrounding air in the fore- or background. With increasing fuel content (i.e. Φ) in the jet, this baseline modestly increases. This is expected, as the refraction index differences between the premixed fuel / air jet and the surrounding air shroud increases. The baseline also increases with turbulent jet Reynolds number due to the more intense mixing between the jet and air shroud, leading to sharper gradients. However, in comparison to the $\sigma_{\nabla J_c}$-values that stem from local mixture stratification, these differences are very subtle and the I_{pm} cases provide a good comparison baseline and optimisation target.

For the non-premixed cases with the simple co-annular tube injector (I_{np}), the existence of separated, locally unmixed, streams is evident by the low $\sigma_{\nabla J_c}$-values in the direct proximity of the injector tip, i.e. z = 4.0 mm. This behaviour is more pronounced for H_2 injection and can be attributed to the comparatively high injection velocity for given Φ (bulk injection velocity range H_2: 25 – 415 m/s, CH_4: 6.2 – 52 m/s). When comparing the mixing performance of I_{np}, three observations are self-evident. i) Under all operating conditions, with the exception of the case CH_4 u_b = 40 m/s, the fully premixed reference line is not reached within the interrogation region of 28 mm (i.e. 4.5D) away from the nozzle exit. This mixing region is critical in the flame stabilisation of H_2-enriched combustion processes in the present piloted [41] as well as related confined configuration [42]. ii) With increasing fuel mass flow rate (top to bottom) from 0.20 ≤ Φ (-) ≤ 2.0, the jet break-up or wrinkling with diverse refraction index gradients is significantly enhanced, yet the stratification at the downstream end increases. iii) The same holds for increasing u_b and thus fuel mass flow rate for a given Φ. Both are attributed to the increased fuel injection momentum and thus penetration depth [43].

By contrast, the space-filling injection concepts approximate the fully premixed reference case line at a

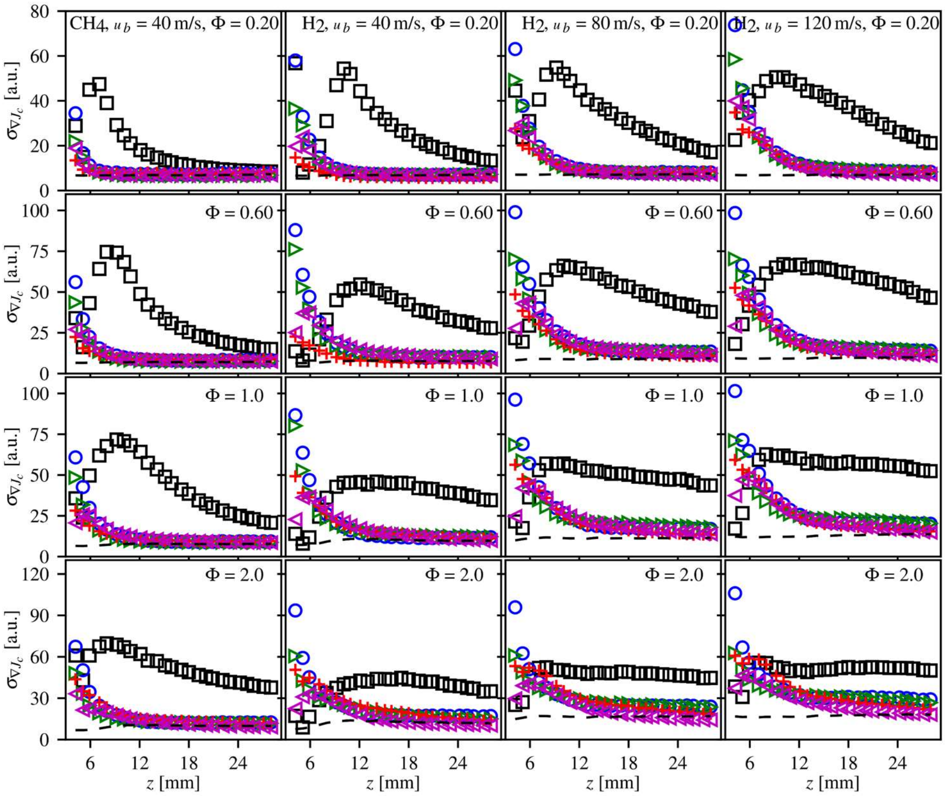

Fig. 6: Standard deviation of the 2D schlieren image gradients ($\sigma_{\Delta Jc}$) for different equivalence ratios $0.20 \leq \Phi \leq 2.0$ (top to bottom), different fuels and u_b (from left to right) and for all injectors. Showing all operating conditions and their mixing progress along approx. 5D from the combustion nozzle tip along the burner symmetry axis ($x = y = 0.0$ mm). The injector is located at $z = 4.0$ mm. The symbols refer to: □ I_{np}; ○ $I_{mt,s}$; ▷ $I_{mt,d}$; + $I_{cr,s}$; ◁ $I_{cr,d}$; - - I_{np}.

certain distance. Inherently, distinct differences are evident in the direct proximity of the injection system within 1-2 mm away from the injector tip. This can be attributed to the different injection orifice positioning. Yet, the injection system differences predominantly diminish within the next 1-2 mm, i.e. $z \leq 8.0$ mm. The initial differences increase with fuel injection momentum (i.e. fuel bulk velocity and Φ).

Methane provides a more compact distribution, due to the lower momentum flux ratio in comparison to H_2, see Table 5. Nonetheless, the data in Fig. 6 show that the designed space-filling injection systems effectively decouple the mixing process from the fuel injection momentum, thus creating excellent fuel and load flexibility in terms of homogenisation performance. To evaluate the injector sensitivity towards fuel mass flow rate further, the data are condensed in Fig. 7, where the maximum differences in $\sigma_{\nabla J_c}$ for the Φ–range are calculated for given z, u_b and fuel, i.e. $\Delta\sigma_{\nabla J_c} | u_b, f$.

The fully premixed case (I_{pm}) presents an approximately equal flat curve through all operating conditions, and serves again as a reference for the comparison with the rest of the injectors, as well as the optimisation target. Please note that a low value of $\Delta\sigma_{\nabla J_c}$ is only indicative of a fuel mass flow rate decoupling and is not related to the mixture homogeneity. For the non-premixed case (I_{np}), a disperse mixture quality distribution is observed in Fig. 6, resulting in elevated $\Delta\sigma_{\nabla J_c}$ values in Fig. 7, hence high Φ sensitivity.

Moreover, and specially for H_2, the curve trend is increasing with z. Thus, in the flame anchoring region,

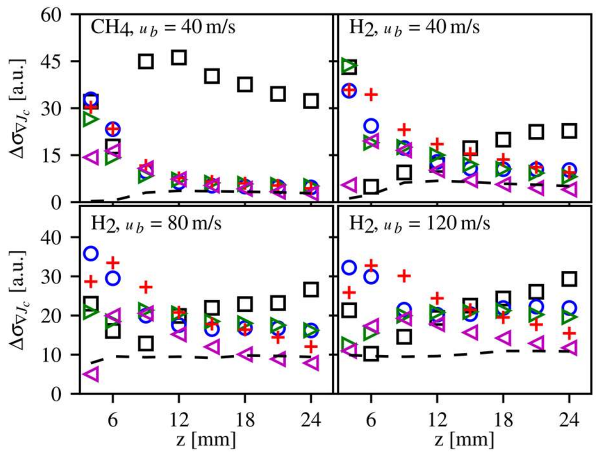

Fig. 7: Maximum ($\Delta\sigma_{\Delta Jc}$) difference between the studied Φ values for CH_4, u_b = 40 m/s (top left); H_2, u_b = 40 m/s (right); H_2, u_b = 80 m/s (bottom left); H_2, u_b = 120 m/s (right). Legend: □ I_{np}; ○ $I_{mt,s}$; ▷ $I_{mt,d}$; + $I_{cr,s}$; ◁ $I_{cr,d}$; - - I_{np}.

the mixture stratification is dependent on the fuel injection momentum. This behaviour is expected due to the co-axial jet injection mechanism at high jet velocity. Consequently, mixing is driven by shear and the break-up of co-axial H_2 jets is difficult [43].

On the other hand, the space-filling injection concepts approximate the fully premixed reference line within the interrogation region. For the CH_4 operating point, a very compact and fast-converging distribution is obtained where fuel injection momentum differences are dissipated within $z/D = 2.0$. The injection of H_2 is noticeably more sensitive towards the fuel mass flow rate with distinct differences between the injectors emerging. This sensitivity is further increasing with fuel mass flow rate, i.e. u_b-variation. Amongst all the micro-injection concepts, the $I_{cr,d}$ design consistently achieves the closest values to the fully premixed reference case. Therefore, it offers the highest load and fuel flexibility, followed by the $I_{cr,s}$, $I_{mt,d}$, and $I_{mt,s}$ respectively. This can be attributed to the randomised injection vector orientation of crown-like injector types.

4.3 Mixture homogenisation length

To quantify a mixing length (l_{mix}) from the schlieren images is somewhat ambiguous. In the current work, it is defined as twice the $\sigma_{\nabla J_c}$ value of the fully premixed reference case. While this definition is, to some degree, arbitrary, it provides a common measure of the mixing length and eliminates the noise associated with the close-to tangential approximation of the tails to the premixed cases. Please note that $l_{mix} / D = 0.0$ corresponds to $z = 4.0$ mm, i.e. injector tip. For methane (see top left panel of Fig. 8), the normalised mixing length moderately increases until $\Phi = 1$, where it appears to stabilise around $l_{mix} / D = 0.8$. This behaviour is shared by all the space-filling injectors. For the non-premixed case I_{np}, the mixing lengths are significantly longer, with only the leanest operating condition reaching the defined criterion within the measurement region (see also Fig. 6). For hydrogen, a similar behaviour is observed. All space-filling injectors achieve the premixed criterion within 1.6 D downstream of the injection point. At a low thermal power (i.e. u_b = 40 m/s with comparatively low fuel mass flow rate) the difference in injection area and resulting jet penetration leads to distinct deviations between the two crown-type injectors, where l_{mix} / D of $I_{cr,s}$ shows a continuous increase with Φ. These injector hardware differences are predominantly diminished for $u_b \geq 80$ m/s and / or higher Φ. As for H_2 injection with I_{np}, the premixed criterion is not reached within the interrogation region.

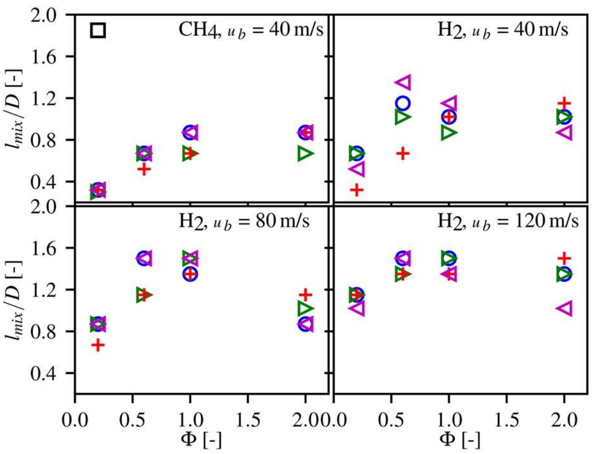

Fig. 8. Mixing length normalised with the injection diameter l_{mix}/D for CH_4, u_b = 40 m/s (top left), H_2, u_b = 40 m/s (right), H_2, u_b = 80 m/s (bottom left) and H_2, u_b = 120 m/s (right). Legend: □ I_{np}; ○ $I_{mt,s}$; ▷ $I_{mt,d}$; + $I_{cr,s}$; ◁ $I_{cr,d}$.

4.4 Pressure loss data

To evaluate the overall performance of the AM space-filling injection concepts, Fig. 9 presents both the pressure loss in the fuel supply and the additional pressure loss caused by obstruction of the combustion air flow around the injection system. The simple tube injector (I_{np}) serves again as reference. It is evident that the fully premixed injection system induces a lower pressure loss to the combustion air, as it is installed into the plenum. However, if a direct injection system is needed, e.g. to mitigate the flashback risks of hydrogen operated combustion systems, the space-filling injection systems induce an increased pressure loss to the combustion air of approximately 100%, or up from 180 mbar to 400 mbar for the high Reynolds number case. This is mostly driven by the overall blockage ratio of the injector to the air flow. However, please note the injection systems have not yet been designed towards low air pressure loss and can be optimised. Obvious solutions are shortened combustor nozzles, placement of the injection system upstream in the cylindrical section and flow optimised injector geometries.

By contrast, distinct differences for the fuel pressure loss across the space-filling injection systems are measured. These scale loosely with the injector opening area, yet the uncertainties in the AM created μ-pores do not facilitate a corresponding correlation. For the crown-type injector with deterministic JiCF holes, ΔP for the high Re case and Φ = 2.0 (i.e. H_2 mass flow rate of 0.12 g/s) a pressure loss of up to 2.0 bar is measured. Under the same operating conditions, the micro-tube family can supply this fuel flow rate at ΔP = 1.4 bar and the crown-type porous injector at around 0.4 bar and thus slightly below the reference tube injector. Under stoichiometric conditions, this pressure loss is readily reduced to about 25%. The pressure loss induced by methane injection follows the same trend, yet is inherently distinctly reduced due to the higher density.

5. Conclusions

In the present study, novel space-filling injection systems have been developed using PBF-LB/M to improve operational performance and fuel flexibility, specifically for optimised mixture homogenisation. A fully premixed and a non-premixed scenario serve as limiting benchmarks. Two distinct AM strategies have been implemented: stochastic porous-media caps for surface injection and deterministic μ-scale jet-in-crossflow configurations. The underlying design hypothesis proposes that employing a sufficient number of injection holes effectively decouples the local fuel mass flow through individual orifices from global mixture stratification phenomena. Consequently, manufacturing tolerances for individual μ-holes can be relaxed, as minor inaccuracies are spatially averaged, thereby enhancing the practicality and robustness of AM injection systems.

The injector performances are investigated using schlieren imaging over a wide range of air flow rate and fuel injection momentum and the mixing homogeneity is evaluated in comparison to the two reference cases.

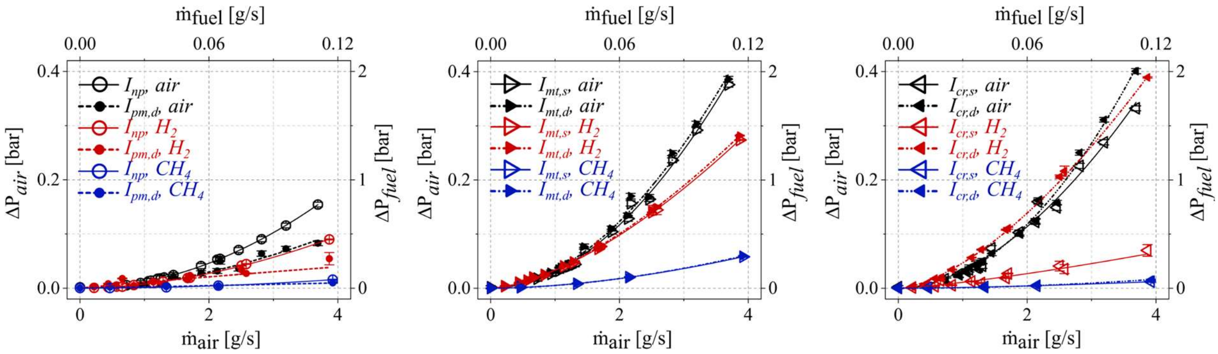

Fig. 9: Pressure drop distribution of the air stream and fuel stream for the different operating conditions. Left: Reference injectors I_{np} and I_{pm}; Middle: I_{mt} in porous surface and deterministic hole variant; Right: I_{cr} in porous surface and deterministic hole variant.

For this purpose, a mixture quality criterion is defined. The symmetry and width of the turbulent structures indicate that both injection mechanism (stochastic pores and deterministic JiCF holes) successfully achieve a homogeneous fuel distribution throughout the entire area. The space-filling injection systems reach this fuel / air mixture homogeneity criterion within 1.6 *D* downstream of the injection point. At this point they also exhibit a distinctly reduced sensitivity towards fuel type (i.e. Wobbe index) and fuel mass flow rate (i.e. Φ or thermal power). This satisfies the hypothesis, that space-filling injection can effectively decouple the mixture formation process from the fuel injection momentum and thus physical fuel properties. This gained control offers the implementation of effective and fuel flexible emission mitigation strategies.

The pressure loss of the fuel supply system is approximately 2-3 times that of the simple open-ended tube, yet with up to 2.0 bar for the highest thermal load manageable. For application in the MGT-sector, the pressure loss to the by-passing combustion air is arguably of bigger concern. Here, the current AM space-filling injection concepts exhibit a ~30% blockage ratio and increase the air pressure loss from 180 mbar to close-to 400 mbar at the highest air flow rate. It is worth noting, that the current project has not focused on optimising the resulting pressure losses and optimisation strategies for practical implementation are proposed.

In general, the develop space-filling injector concepts fully capitalise on function integration of AM processes and carry high potential to combine the safety aspects of direct injection systems, e.g. for H_2 operation, with the benefits of partially premixed combustion including the omission of mixture stratification associated hot spots that drive the formation of thermal NO_X. The development of the current injector configurations is focused on the spatial requirements of jet stabilised MGT systems due to the AM-related challenges when creating µ-structures in conventional PBD/LB-M. However, these principles are directly transferable and scalable to larger gas turbines. Generally, improved mixing yields reduced emissions. The short mixing timescales are particularly beneficial for H_2 combustion systems that require direct injection to mitigate boundary layer flashback. While the benefits in mixture formation are clear, the effects on the emission performance and combustion stability need to be assessed thoroughly prior to the integration into practical GT burners. Future work shall focus on expanding the Wobbe index flexibility to partially cracked ammonia injection, evaluating the benefits of AM space-filling injection concepts in terms of combustion and emission performance, and co-optimise the designs for pressure drop using numerical DoE techniques and test them in a more realistic environment with high pressure and temperature.

Declaration of competing interest
Nothing to declare.

Acknowledgements
The authors acknowledge the funding by the Deutsche Forschungsgemeinschaft (DFG, German Research Foundation) - project numbers: 523873650.

Data availability
Data will be made available on request.

Author contribution statement
Vicente Rubio: Writing – original draft, Writing – review & editing, Investigation, Visualization. **Jihwan Ahn:** Writing – review & editing, Investigation, Visualization. **Clemens Maucher:** Writing – review & editing, Validation. **Hans-Christian Möhring:** Resources, Funding acquisition. **Fabian Hampp:** Conceptualization, Investigation, Methodology, Formal analysis, Writing – original draft, Writing – review & editing, Visualization, Supervision, Project administration, Funding acquisition, Resources, Software.

References

1. T.C. Lieuwen, V. Yang, Gas Turbine Emissions, (Cambridge University Press, 2013)
2. T.C. Lieuwen, V. McDonell, E. Petersen, D. Santavicca, Fuel Flexibility Influences on Premixed Combustor Blowout, Flashback, Autoignition, and Stability, J. Eng Gas Turb. Power **130**, 011506 (2008) https://doi.org/10.1115/1.2771243
3. N. Qasem, A. Mourad, A. Abderrahmane, Z. Said, O. Younis, K. Guedri, L. Kolsi, A recent review of aviation fuels and sustainable aviation fuels, J Therm. Anal. Calorim. **149**, 4287-4312 (2024) https://doi.org/10.1007/s10973-024-13027-5
4. B. Emerson, S.J. Patel, S. Gubbi, R.G. McKinney, D. Wu, D.R. Noble, T.C. Lieuwen, Nonpremixed Approaches for Fuel Flexible, Low NOx Combustors in High-Efficiency Gas Turbines in Proc. ASME Turbo Expo, London, UK, June 24-28, (2024), GT2024-129213 https://doi.org/10.1115/GT2024-129213
5. O. Agwu, A. Valera-Medina, T. Katrašnik, T. Seljak, Flame characteristics of glycerol/methanol blends in a

swirl-stabilised gas turbine burner, Fuel **290**, 119968 (2021) https://doi.org/10.1016/j.fuel.2020.119968
6. M. Stefanizzi, T. Capurso, G. Filomeno, M. Torresi, G. Pascazio, Recent Combustion Strategies in Gas Turbines for Propulsion and Power Generation toward a Zero Emissions Future: Energies **14**, 6694 (2021) https://doi.org/10.3390/en14206694
7. Z. Li, Y. Zhang, H. Zhang, Kinetics modeling of NOx emission of oxygen-enriched and rich-lean staged ammonia combustion under gas turbine conditions, Fuel **355**, 129509 (2024) https://doi.org/10.1016/j.fuel.2023.129509
8. O. Awad, B. Zhou, K. Harrath, K. Kadirgama, Characteristics of NH3/H2 blend as carbon-free fuels: A review, Int. J. Hydrog. Energ. **48**, 38077-38100 (2023) https://doi.org/10.1016/j.ijhydene.2022.09.096
9. A. Cavaliere, M. Joannon, Mild Combustion, Prog. Energ. Combust. Sci. **30**, 329-366 (2004) https://doi.org/10.1016/j.pecs.2004.02.003
10. O. Lammel, H. Schutz, G. Schmitz, R. Lückerath, M. Stöhr, B. Noll, M. Aigner, M. Hase, W. Krebs, FLOX® Combustion at High Power Density and High Flame Temperatures, J. Eng Gas Turb. Power **132**, 121503 (2010). https://doi.org/10.1115/1.4001825
11. H. Nozari, G. Karaca, O. Tuncer, A. Karabeyoglu, Porous medium based burner for efficient and clean combustion of ammonia-hydrogen air systems, Int. J. Hydrog. Energ. **42**, 14775-14785 (2017) https://doi.org/10.1016/j.ijhydene.2017.03.234
12. R. Banihabib, M. Assadi, The Role of Micro Gas Turbines in Energy Transition, Energies **15**, 8084 (2022) https://doi.org/10.3390/en15218084
13. I. Waitz, G. Gauba, Y.S. Tzeng, Combustors for Micro-Gas Turbine Engines, J. Fluids Eng. **120**, 109-117 (1998) https://doi.org/10.1115/1.2819633
14. X. Liu, W. Shao, Y. Liu, Y. Tian, Z. Zhang, Y. Xiao, G. Kraemer, Cold flow characteristics of a novel high-hydrogen Micromix model burner based on multiple confluent turbulent round jets, Int. J. of Hydrog. Energ. **46**, 5776-5789 (2021) https://doi.org/10.1016/j.ijhydene.2020.11.012
15. X. Liu, W. Shao, Y. Liu, Y. Tian, Z. Zhang, Y. Xiao, Investigation of H2/CH4-Air Flame Characteristics of a Micromix Model Burner at Atmosphere Pressure Condition in Proc. ASME Turbo Expo, Oslo, Norway, June 11-15, (2018), GT2018-76276 https://doi.org/10.1115/GT2018-76276
16. C. Xing, X. Chen, P. Qiu, L. Liu, X. Yu, Y. Zhao, L. Zhang, J. Liu, Q. Hu, Effect of fuel flexibility on combustion performance of a micro-mixing gas turbine combustor at different fuel temperatures, J. Energy Inst. **102**, 100-117 (2022) https://doi.org/10.1016/j.joei.2022.02.010
17. S. Hernandez, Q. Wang, V. McDonell, A. Mansour, E. Steinthorsson, B. Hollon, Micro Mixing Fuel Injectors for Low Emissions Hydrogen Combustion in Proc. ASME Turbo Expo, Berlin, Germany, June 09-13, (2008), GT2008-50854 https://doi.org/10.1115/GT2008-50854
18. A. Horikawa, K. Okada, M. Yamaguchi, S. Aoki, M. Wirsum, H. Funke, K. Kusterer, Combustor Development and Engine Demonstration of MicroMix Hydrogen Combustion Applied to M1A-17 Gas Turbine in Proc. ASME Turbo Expo, Virtual, June 07-11, (2021), GT2021-59666, https://doi.org/10.1115/GT2021-59666
19. B. Hollon, E. Steinthorsson, A. Mansour, V. McDonell, H. Lee, Ultra-Low Emission Hydrogen/Syngas Combustion With a 1.3 MW Injector Using a Micro-Mixing Lean-Premix System in Proc. ASME Turbo Expo, Vancouver, BC, Canada, June 06-10, (2011), GT2011-45929 https://doi.org/10.1115/GT2011-45929
20. R. Zhu, W. Weng, S. Liu, W. Wang, Y. He, Z. Wang, Flame stability and NOx emission characteristics of a high H2-content CH4/H2 fueled micro-mixing burner, Fuel **375**, 132506 (2024). https://doi.org/10.1016/j.fuel.2024.132506
21. A. Landry-Blais, S. Sivić, M. Picard, Micro-Mixing Combustion for Highly Recuperated Gas Turbines: Effects of Inlet Temperature and Fuel Composition on Combustion Stability and NOx Emissions, J. Eng. Gas Turb. Power **144**, 091014 (2022) https://doi.org/10.1115/1.4055190
22. H. Funke, N. Beckmann, J. Keinz, A. Horikawa, 30 Years of Dry-Low-NOx Micromix Combustor Research for Hydrogen-Rich Fuels—An Overview of Past and Present Activities, J. Eng. Gas Turb. Power **143**, 071002 (2021) https://doi.org/10.1115/1.4049764
23. T. Pereira, J.V. Kennedy, J. Potgieter, A comparison of traditional manufacturing vs additive manufacturing, the best method for the job, Proc. Manuf. **30**,11-18 (2019) https://doi.org/10.1016/j.promfg.2019.02.003
24. B.P. Conner, G.P. Manogharan, A.N. Martof, L.M. Rodomsky, C.M. Rodomsky, D.C. Jordan, J.W. Limperos, making sense of 3-D printing: Creating a map of additive manufacturing products and services, Addit. Manuf. **1-4**, 64-76 (2014) https://doi.org/10.1016/j.addma.2014.08.005
25. C. Sun, Y. Wang, M. McMurtrey, N. Jerred, F. Liou, J. Li, Additive manufacturing for energy: A review, Appl. Energ. **282**, 116041 (2021) https://doi.org/10.1016/j.apenergy.2020.116041
26. C. Maucher, Y. Kang, S. Bechler, M. Ruf, H. Steeb, H.C. Möhring, F. Hampp, Towards bespoke gas permeability by functionally graded structures in laser-based powder bed fusion of metals, Addit. Manuf. **94**, 104466 (2024) https://doi.org/10.1016/j.addma.2024.104466
27. U. Bhayaraju, M. Hamza, Development of Porous Injection Technology to Reduce Emissions for Dry Low NOx Combustors: Micromixer and Swirl Injectors in Proc. ASME Turbo Expo, Charlotte, NC, USA, June 26-30, (2017), GT2017-63976 https://doi.org/10.1115/GT2017-63976
28. Y. Kang, J. Seidler, J. Ahn, V. Rubio, C. Maucher, H.C. Möhring, F. Hampp, AM microstructures with bespoke permeability, Int. J. Heat Mass Trans **241**, 126674 (2025) https://doi.org/10.1016/j.ijheatmasstransfer.2025.126674
29. A. Adamou, J. Turner, A. Costall, A. Jones, C. Copeland, Design, simulation, and validation of additively manufactured high-temperature combustion chambers for micro gas turbines, Energ. Convers. Manage. **248**, 114805 (2021) https://doi.org/10.1016/j.enconman.2021.114805
30. G. Settles, M. Hargather, A review of recent developments in schlieren and shadowgraph techniques, Meas. Sci. Technol **28**, 042001 (2017) https://doi.org/10.1088/1361-6501/aa5748
31. W. S. Chai, Y. Bao, P. Jin, G. Tang, L. Zhou, A review on ammonia, ammonia-hydrogen and ammonia-methane fuels, Renew. Sust. Energ. Rev. **147**, 111254 (2021) https://doi.org/10.1016/j.rser.2021.111254
32. David R. Lide, ed., CRC Handbook of Chemistry and Physics, Internet Version 2005, CRC Press, Boca Raton, FL, 2005.
33. J. Zachariah-Wolff, T. Egyedi, K. Hemmes, From natural gas to hydrogen via the Wobbe index: The role of standardized gateways in sustainable infrastructure

transitions, Int. J. Hydrog. Energ. **32**, 1235-1245 (2006) https://doi.org/10.1016/j.ijhydene.2006.07.024

34. A. Valera-Medina, D.G. Pugh, P. Marsh, G. Bulat, P. Bowen, Preliminary study on lean premixed combustion of ammonia-hydrogen for swirling gas turbine combustors, Int. J. Hydrog. Energ. **42**, 24495-24503 (2017) https://doi.org/10.1016/j.ijhydene.2017.08.028
35. Y. Kang, J. Ahn, F. Hampp, Low Swirl Effect on Compact Spray and Combustion Systems Using Additive Manufactured Dual Airblast Injectors, J. Eng Gas Turb. Power **32**, 121001 (2024) https://doi.org/10.1115/1.4066005
36. G.S. Settles, A. Liberzon, Schlieren and BOS velocimetry of a round turbulent helium jet in air, Opt Laser Eng. **156**, 107104 (2022) https://doi.org/10.1016/j.optlaseng.2022.107104
37. D. Kroon, Numerical optimization of kernel based image derivatives, Short Paper University Twente **3**, 5 (2009)
38. C. Eichler, G. Baumgartner, T. Sattelmayer, Experimental Investigation of Turbulent Boundary Layer Flashback Limits for Premixed Hydrogen-Air Flames Confined in Ducts, J. Eng. Gas Turbines Power **134**, 011502 (2012) https://doi.org/10.1115/1.4004149
39. C. Ezenwajiaku, R. Balachandran, A. Ducci, M. Picciani, M. Talibi, Experimental Characterisation of the Dynamics of Partially Premixed Hydrogen Flames in a Lean Direct Injection (LDI) Combustor in Proc. ASME Turbo Expo, Boston, Ma, USA, June 26-30, (2023), GT2023-102611, https://doi.org/10.1115/GT2023-102611
40. A. Sukhodolov, T. Sukhodolova, Dynamics of Flow at Concordant Gravel Bed River Confluences: Effects of Junction Angle and Momentum Flux Ratio, J. Geophys. Res. Earth Surf. **124**, 588-615 (2019) https://doi.org/10.1029/2018JF004648
41. N. Petry, M. Mannazhi, Z. Yin, O. Lammel, K.P. Geigle, A. Huber, Investigation of Fuel and Load Flexibility of an Atmospheric Single Nozzle Jet-Stabilized FLOX® Combustor with Hydrogen/Methane-Air Mixtures, J. Eng Gas Turb. Power **146**, GTP-23-1439 (2023) https://doi.org/10.1115/1.4063782
42. J. Ahn, F. Hampp, Hydrogen-enriched combustion at high preheat conditions, 13^{th} Med. Combust. Symp. (2025) MCS13-147-COL15.
43. F. Duronio, A. De Vita, CFD analysis of hydrogen and methane turbulent transitional under-expanded jets, Int. J. Heat Fluid Flow **107**, 109381 (2024) https://doi.org/10.1016/j.ijheatfluidflow.2024.109381